

# P(VDF-TrFE) nanocomposite thin films with cellulose nanofibers and dopamine-modified BaTiO<sub>3</sub> nanoparticles for enhanced energy storage

Davide Disnan<sup>a</sup>, Michael Schneider<sup>a</sup>, Xinxin Zhang<sup>b</sup>, Kunpeng Qian<sup>b</sup>, Fabian Bacher<sup>a</sup>, Yin Zhao<sup>b</sup>, Xin Feng<sup>b</sup> and Ulrich Schmid<sup>a</sup>

<sup>a</sup>Institute of Sensor and Actuator Systems, TU Wien, Vienna, Austria; <sup>b</sup>Department of Chemistry, Research Center of Nano Science and Technology, Shanghai University, Shanghai, China

## ABSTRACT

Fluoropolymers, known for their high dielectric permittivity, are extensively studied for nanocomposite energy storage. However, nanoparticle incorporation introduces defects, making the fabrication of thin films able to withstand high electric fields challenging. Consequently, research on films thinner than 10  $\mu\text{m}$  remains limited, despite their potential for effective polarization at lower voltages. Among fluoropolymers, P(VDF-TrFE) offers well-established and easy thin film deposition *via* spin coating, making it ideal for nanocomposite thin films. This study presents the synthesis and energy storage characterization of P(VDF-TrFE) nanocomposite thin films with a thickness of  $\sim 1 \mu\text{m}$ , demonstrating enhanced energy storage performance. This is achieved by adding a nanoparticle mixture of carboxymethyl cellulose nanofibers and polydopamine-coated BTO into the P(VDF-TrFE) polymer matrix, resulting in a 60% increase in energy density and a twofold enhancement in energy efficiency. A direct correlation between the nanoparticle concentration and the observed enhancements in dielectric and ferroelectric characteristics is established.

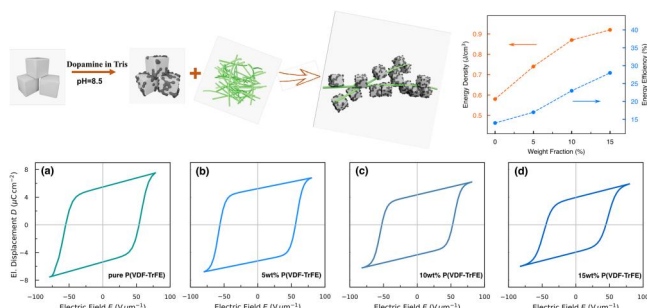
## ARTICLE HISTORY

Received 29 July 2024  
Accepted 10 March 2025

## KEYWORDS

P(VDF-TrFE); energy storage; nanocomposite; barium titanate; nanocellulose; polydopamine; ferroelectricity; thin films



## GRAPHICAL ABSTRACT




## Introduction

In recent years, extensive research has been devoted to polymer-based dielectric nanocomposite, driven by the increasing importance of improving their electrical and optical properties, coupled with low

production costs and ease of processing. Even more, the integration of nanofillers into a polymer matrix has significantly enhanced the performance of various polymers, including poly(methyl methacrylate) (PMMA), polydimethylsiloxane (PDMS) and

**CONTACT** Davide Disnan  [davide.disnan@tuwien.ac.at](mailto:davide.disnan@tuwien.ac.at)  Institute of Sensor and Actuator Systems, TU Wien, Gusshausstrasse 27-29, 1040 Vienna, Austria

 Supplemental data for this article can be accessed online at <https://doi.org/10.1080/20550324.2025.2479392>.

© 2025 The Author(s). Published by Informa UK Limited, trading as Taylor & Francis Group.

This is an Open Access article distributed under the terms of the Creative Commons Attribution License (<http://creativecommons.org/licenses/by/4.0/>), which permits unrestricted use, distribution, and reproduction in any medium, provided the original work is properly cited. The terms on which this article has been published allow the posting of the Accepted Manuscript in a repository by the author(s) or with their consent.

polyimides, particularly in biomedical, optical, wearable and sensor applications [1–8]. Due to their high breakdown strength, polymers are also an excellent choice for energy storage applications. However, their relatively low dielectric permittivity, typically ranging from 2 to 4, imposes limitations on the energy density performance [9]. But, within the broad category of polymers, there exists a distinctive subset known as polar polymers. This latter group of materials is characterized by individual dipole moments, resulting in a higher dielectric constant compared to their nonpolar counterparts [10]. This inherent polarity has led to the wide investigation into ferroelectric polymers like poly(vinylidene fluoride) (PVDF) and its co-polymers (e.g. poly(vinylidene fluoride-trifluoroethylene) (P(VDF-TrFE))), which show a relatively high permittivity of  $\sim 10$ . To further enhance the material's energy density, incorporating nanofillers with dielectric constant orders of magnitude higher into PVDF-based polymers has emerged as a topic of significant investigation [11–14]. However, there are several physical limitations associated with this approach. For instance, surpassing a certain threshold in filler loading can lead to nanoparticle agglomerations due to their high surface energy, potentially reducing the overall dielectric breakdown strength of the composite material and the polarization area. Additionally, the typically significant difference in dielectric constants between the fillers and the matrix results in local inhomogeneity of the electric field at the interface between both materials [9,10,15]. In nanocomposites, the Maxwell-Wagner-Sillar interfacial polarization between nanofiller and matrix is observed [16–18]. According to this model, current flow across an interface between two dielectric materials with different relaxation times results in charge accumulation at the interface. If the nanoparticles are not well dispersed within the polymer matrix, this can lead to an uneven electric field distribution, which can considerably reduce the breakdown strength. Another challenge is the chemical incompatibility between the organic polymer matrix and the surface of the integrated inorganic nanofiller which can create voids and pores, further contributing to a locally inhomogeneous electric field distribution [9]. To address these limitations, various nanoparticle surface modifications have been proposed. One solution is placing a highly insulating buffer layer with a low dielectric constant at the interface between the filler and the polymer matrix as a double core-shell structure to achieve a more uniform electric field distribution [19]. Furthermore, enhanced compatibility between the polymer matrix and the filler is also achieved through other surface modifications, including hydrogen peroxide [20–22],

phosphonic acid [23], titanate coupling agent [24], and polydopamine [25]. Polydopamine, due to its ease of use, cost-effectiveness, sustainability, environmental compatibility, and ability to be deposited on virtually all types of inorganic and organic surfaces [26–28], has found widespread use in functionalizing various substrates since its introduction in 2007 [29]. These applications range from polymeric nanoparticles [30] and nanodiamonds [31] to ceramics [32] and graphene [33].

Organic nanoparticles, such as cellulose-based nanoparticles as fillers are commonly employed in various applications [34–36]. Cellulose, the most ubiquitous and abundant biopolymer in nature, has attracted significant attention for both its biosynthesis and applications in the form of nanoparticles [36]. Cellulose nanofibers, in particular, have already demonstrated their effectiveness as a green binder for a variety of composite polymer materials. This is attributed to their high crystallinity, unique long polymer chain molecular structure, abundant surface functional groups, and subtle physiochemical properties [37]. Moreover, previous studies have shown that cellulose nanofibers can increase the crystallinity and relative fraction of the piezoelectric  $\beta$ -phase of PVDF and thus improve the piezoelectricity of polymer composites [38]. Recent advancements in the field of energy storage devices have highlighted the potential of cellulose-based nanocomposites [39]. Additionally, the literature indicates that the introduction of cellulose nanocrystals in PVDF-based nanocomposites contributes to an increased dielectric constant [40].

Publications focusing on the energy characteristics of PVDF-based nanocomposite primarily center on relatively thick polymer films, typically ranging between 10 and 40  $\mu\text{m}$  [11,12,41–43]. While thick films offer higher robustness to environmental conditions and higher stability, they may not be suitable for instance in applications requiring large specific surface areas [44–46]. Additionally, such thick films require extremely high voltages, typically in the kilovolt (kV) range, for effective polarization of the polymer films. The breakdown strength of polymeric materials is thickness-dependent, with thinner dielectric polymers withstanding higher voltages, according to a theoretical model based on space charge dynamics [47]. However, thin polymer layers are more susceptible to processing defects, such as pits, dimples, contaminants, roughness, wrinkles, and variable thickness. As a result, experimentally dielectric breakdown strength does not consistently increase with decreasing thickness, making these films more susceptible to localized breakdown. In literature, a thickness threshold for achieving high dielectric strength is typically found around 10  $\mu\text{m}$

[48]. Consequently, a noticeable gap in the literature exists in the study of energy characteristics in PVDF-based nanocomposites with a film thickness below 10  $\mu\text{m}$ . To the best of the authors' knowledge, there has been only one investigation into PVDF-based nanocomposite thin films with a thickness below 2  $\mu\text{m}$  including ferroelectric characterization, with a maximum nanofiller content of only 2% in weight [49].

In this study, we investigate the energy characteristics of P(VDF-TrFE) nanocomposite thin films which are loaded with polydopamine-functionalized BaTiO<sub>3</sub> nanoparticles mixed with nanocellulose fibers. The analyzed thin films in this report have a thickness of  $\sim 1 \mu\text{m}$ , rendering them suitable for applications demanding polarization at moderate voltage levels. X-ray diffraction (XRD) analysis revealed the influence of the introduction of these nanofillers in the P(VDF-TrFE) matrix on the ferroelectric  $\beta$ -phase, subsequently confirmed by ferroelectric characterization. Furthermore, to explore energy storage applications, we measured the permittivity and the dielectric characteristics as a function of frequency. The electrical properties were studied by examining the electrical displacement as a function of the electric field and determining the ferroelectric characteristics, such as coercive field and remnant polarization. Our measurements reveal the improvements in energy density achieved through the introduction of BTO@PDA mixed with CCNF nanofillers, with nanofiller concentrations of up to 15% by weight. This achievement, not previously reported in the literature for such thin films, underscores the feasibility of nanocomposite thin films in energy storage applications.

## Experimental details

### Materials

BaTiO<sub>3</sub> (BTO) powder was prepared by a hydrothermal method [50]. Dopamine hydrochloride (DA) powder was obtained from Sinopharm Group Chemical Reagent Co., LTD. The carboxyl cellulose nanofibers (CCNF) with a solid content of 3% in weight were obtained *via* ammonium sulfate (APS) oxidization method by using cotton fiber as source materials based on previous literature [51]. Tris (hydroxymethyl) aminomethane was bought from Adamas Reagent Co., LTD. Deionized (DI) water was also used during the experimentation. P(VDF-TrFE) was purchased from Piezotech/Arkema Group. 2-butanone (methyl ethyl ketone (MEK)) was obtained from Technic France.

### Preparation of CCNF-BTO@PDA

The BTO@PDA was prepared by BTO powder and DA powder in tris buffer solution at a pH value of 8.5. Specifically, 45 g BTO powder, 2.25 g DA powder, and 300 ml tris buffer solution at pH = 8.5 were magnetically stirred for 24 h. In this process, polydopamine (PDA) was obtained by self-polymerization of DA. Then BTO@PDA solution was subjected to high-speed centrifugation for 10 min for 5 times, and the upper liquid of the BTO@PDA solution was removed. The wet sediment composed of BTO@PDA at the bottom of the centrifuge tube was further treated by ultrasonication for 1 h and then transferred to the CCNF solution by intensive mixing with magnetic stirring for 12 h. Subsequently, the CCNF-BTO@PDA wet sediments were obtained by washing and centrifuging with deionized water for 5 min at 10000 rpm twice. A representation of the CCNF-BTO@PDA is reported in Figure 1a. Standard CNF possesses a strong tendency to self-association due to interactions between surface hydroxyl groups, leading to nanofiller aggregation and challenging homogenous dispersion, which negatively impacts energy storage characteristics. To overcome this, CCNF is used, replacing hydroxyl groups with carboxymethyl groups, thereby improving dispersibility [52].

### Synthesis of nanocomposite thin films

The nanocomposite thin films were prepared with CCNF-BTO@PDA nanoparticles as fillers at different weight fractions of 5%, 10%, and 15%, respectively. P(VDF-TrFE) powder with a ratio VDF/TrFE of 70:30 mol% was used as a matrix for fabricating the nanocomposite thin films. The polymer powder was added with a weight ratio of 8% into the solvent MEK at 50 °C to increase the dissolution rate. The resulting polymer solution was subject to magnetic stirring until a homogenous solution was achieved. Subsequently, the nanoparticles were uniformly dispersed in the polymer solution in quantities corresponding to the previously reported weight fraction. This dispersion process was enabled with a sonicator (UP400S from Hielscher) for 1.5 h, and an external water-cooling system to prevent MEK solvent evaporation. Next, the nanocomposite thin films were deposited *via* spin-coating at 2000 rpm, resulting in homogenous thin films, which were annealed in air for 2 h at 140 °C to enhance their crystallinity. Afterwards, the nanocomposite thin films were cooled down to room temperature on the hot plate. Spin-coating and annealing were carried out under humidity-controlled conditions. Due to the polar nature of MEK as the solvent, maintaining a humidity level below

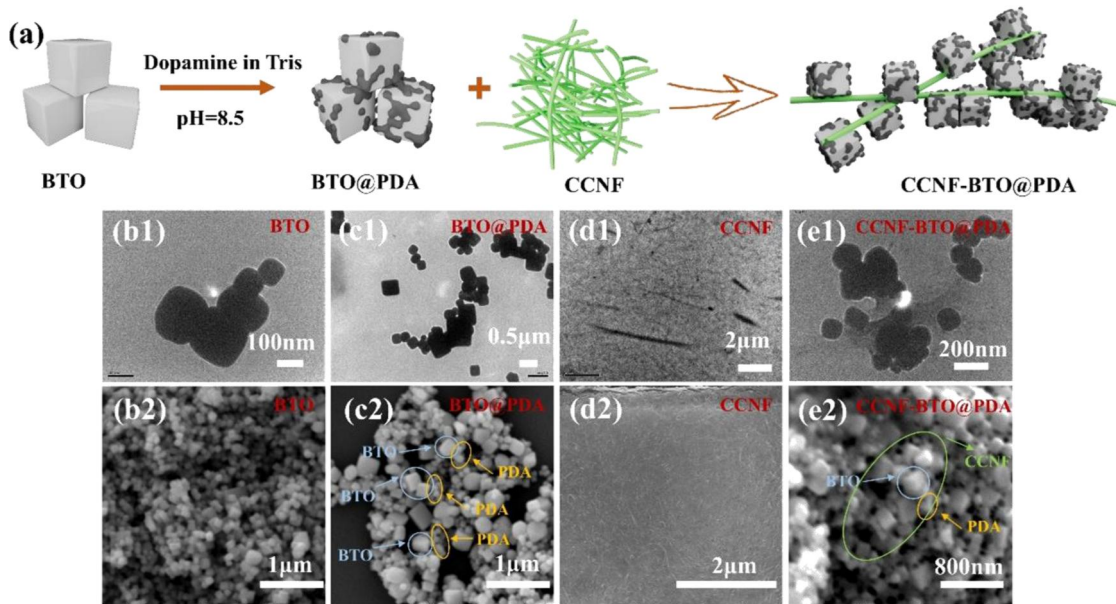


**Figure 1.** Preparation and electron microscope images of the nanoparticles. (a) Schematic process flow of the CCNF-BTO@PDA fabrication. TEM and SEM images of (b1,b2) BTO, (c1,c2) BTO@PDA, (d1,d2) CCNF, and (e1,e2) CCNF-BTO@PDA.

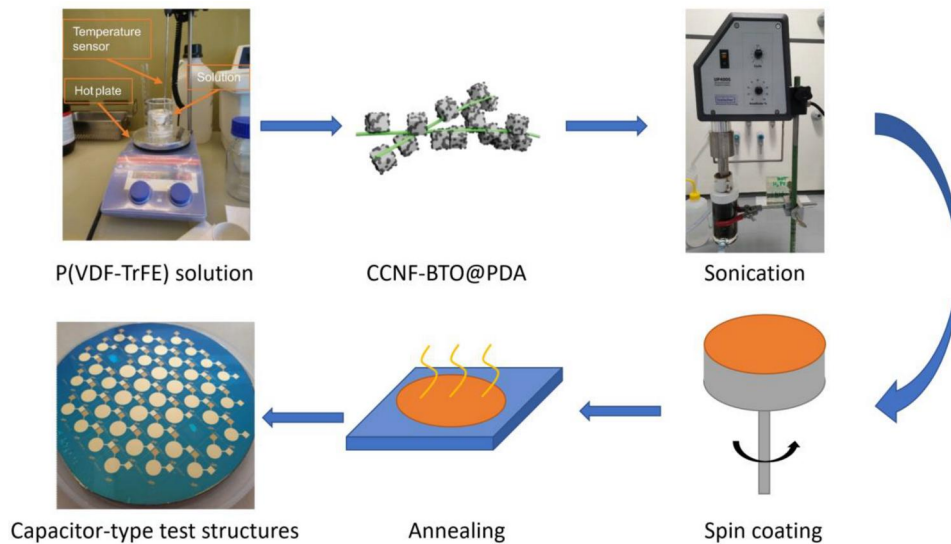


**Figure 2.** Schematic illustration of nanocomposite thin film synthesis. The CCNF-BTO@PDA nanoparticle mixture is added to the 8% weight ratio P(VDF-TrFE) polymer solution. After sonication, the nanocomposite thin film is deposited *via* spin coating and then annealed at 140 °C for 2 h. The resulting capacitor-type test structures are presented.

10% is important to prevent potential vapor-induced phase separation during the fabrication process and to ensure the reproducibility of layer quality [53]. The whole process is represented in Figure 2. The final film thickness was measured to  $1.2 \pm 0.1 \mu\text{m}$  for each sample using a DEKTAK surface profilometer.

#### **Fabrication of the metal-nanocomposite-metal capacitors**

For measuring the permittivity and studying the energy characteristics of the nanocomposite thin film, micromachined circular-shaped capacitors with 6 mm of diameter were fabricated. The metal-

nanocomposite-metal structure was developed starting from a 4" (100) Si wafer with 500 nm thermal silicon dioxide ( $\text{SiO}_2$ ), needed for electrical insulation. The bottom electrode was formed by a lift-off process, consisting of a 50 nm chromium (Cr) layer by electron-beam evaporation serving as an adhesion promoter for a 150 nm thermally evaporated gold (Au) layer. Afterwards, the nanocomposite thin films were spin-coated from the solution, according to the procedure discussed above, and annealed. For top electrode realization, a 150 nm Au layer was thermally evaporated and subsequently patterned by wet chemical etching to serve as the top electrode. Details about microfabrication can be found elsewhere [54].

### Characterization of nanoparticles

The morphology and microstructure of the nanoparticles were observed by scanning electron microscope (SEM, Phenom XL, The Netherlands) and transmission electron microscope (TEM, 120 kV, JEM200-CX, Japan). The surface height images of the nanoparticles were measured by an atomic force microscope (AFM, Park XE7, Park Systems, Korea). X-ray diffraction (XRD) patterns were obtained with a multi-functional X-ray diffractometer (SmartLab, Japan) from  $5^\circ$  to  $60^\circ$  with a scan speed of  $20^\circ/\text{min}$ . The chemical compositions were investigated using an infrared spectrometer (FTIR, Nicolet 380, USA) with wavenumbers ranging from  $400$  to  $4000\text{ cm}^{-1}$ .

### Characterization of nanocomposite thin films

The chemical composition, as well as the presence of crystalline phase in the nanocomposite thin films, were detected with a Fourier transform infrared (FTIR) spectrometer (Bruker Tensor 27) from  $1500\text{ cm}^{-1}$  to  $700\text{ cm}^{-1}$  in absorbance mode and with an X-ray diffractometer (XRD) (X'Pert Pro from Malvern Panalytic) in Bragg-Brentano configuration with a  $\text{Cu-K}_{\alpha 1-2}$  source at wavelengths of  $1.540598\text{ \AA}$  and  $1.54426\text{ \AA}$ , respectively. The dielectric constant and characteristics of the nanocomposite thin films were measured using an LCR meter IM3533-01 (Hioki). The polarization within the material as a function of the electric field was measured *via* a Sawyer-Tower circuit [54]. A 100 Hz triangular wave AC signal was applied to the micromachined capacitor and the amplitude was incrementally increased. This allowed us to observe the typical hysteretic behaviour, enabling the evaluation of parameters such as the coercive field ( $E_c$ ) and the remnant polarization ( $P_r$ ).

## Results and discussion

### Characteristics and structure of nanoparticles

Analysis with SEM and TEM images in Figure 1 revealed that the BTO particles exhibited a typical cube morphology, as shown in Figure 1(b1,b2), with an average particle size of  $\sim 145\text{ nm}$  (Supplementary Figure 1). This size was targeted to maximize the dielectric permittivity benefits associated with nanoparticle size [55]. When combined with PDA, BTO is enveloped by PDA (BTO@PDA) (Figure 1(c1,c2)). By further mixing in carboxymethyl cellulose nanofibers (CCNF) (Figure 1(d1,d2)), it can be observed that particulate BTO@PDA is dispersed within the fibrous network (Figure 1(e1,e2)). The additional evidence of the successful integration of CCNF, BTO, and PDA is also highlighted in Figure 3(a1–a4),(b1–b4)).

The SEM and TEM images, shown in Figures 2, 3, prove the high process compatibility of BTO, PDA, and CCNF. The XRD patterns of both pure BTO and BTO@PDA (Figure 4a) exhibited characteristic diffraction peaks typical of BTO's crystallographic microstructure [56], consistent with the standard card JCPDS (No. 75-0213) [57]. The XRD pattern of BTO@PDA remained unchanged after functionalization, indicating that the crystal structure of BTO was unaltered by the addition of PDA [58]. The characteristic peaks presented in Figure 4a at  $16^\circ$ ,  $22.7^\circ$ , and  $34.5^\circ$  correspond to the (110), (200) and (004) lattice plane of CCNF, respectively [59]. After loading with CCNF, the XRD pattern of CCNF-BTO@PDA was attributed to the polymer CCNF, where the distinct diffraction peaks of (110) and (200) became less prominent due to the high crystallinity of BTO. The corresponding FTIR spectrum is shown in Figure 4b,c. Comparing BTO with BTO@PDA, new characteristic absorption peaks at  $1291\text{ cm}^{-1}$  and  $1625\text{ cm}^{-1}$  were observed in BTO@PDA, attributed to the bending and stretching vibrational modes of -C-O and -N-H bonds in PDA, demonstrating that BTO was successfully modified by PDA [60]. In addition, the wide characteristic absorption peak at  $3432\text{ cm}^{-1}$  of -OH and -NH bonds proved the existence of hydrogen bond interaction between PDA and BTO. With the introduction of CCNF, CCNF-BTO@PDA inherited all the characteristic absorption peaks of CCNF, especially the absorption peak at  $1730\text{ cm}^{-1}$  was attributed to the C=O stretching vibration of -COOH in CCNF, which indicated the successful introduction of CCNF [61]. Moreover, compared with pure CCNF infrared spectrum, the absorption peak of CCNF-BTO@PDA blue shifts from  $1060\text{ cm}^{-1}$  to  $1026\text{ cm}^{-1}$ , which may be due to the hydrogen bond interaction and the physical electrostatic interaction between CCNF (-COOH) and PDA (-OH) [62]. All results presented above prove the successful preparation of CCNF-BTO@PDA.

### Crystalline phase and microstructure of the nanocomposite thin films

Figure 5a presents the FTIR spectra of pure P(VDF-TrFE) as well as nanocomposite thin films loaded with different CCNF-PDA@BTO concentrations. Worth noting that no discernible new absorption peaks emerge in the nanocomposite films. According to the FTIR analysis, the addition of CCNF-PDA@BTO nanoparticles does not alter the chain conformation of the P(VDF-TrFE) matrix. From the spectra, we can identify two strong absorption bands at  $850\text{ cm}^{-1}$  and  $1277\text{ cm}^{-1}$ , which can be attributed to the  $\text{CF}_2$  vibration and  $\text{CH}_2$

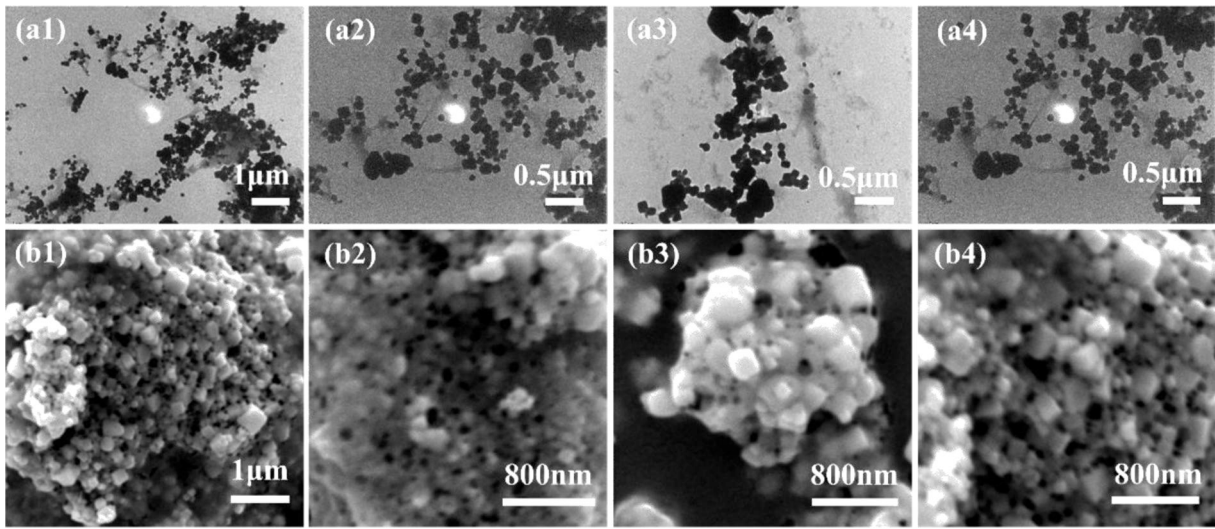


**Figure 3.** SEM and TEM images of the nanoparticles. (a1–a4) TEM and (b1–b4) SEM images of CCNF-BTO@PDA show the successful integration of the cellulose fibers with the BTO@PDA.

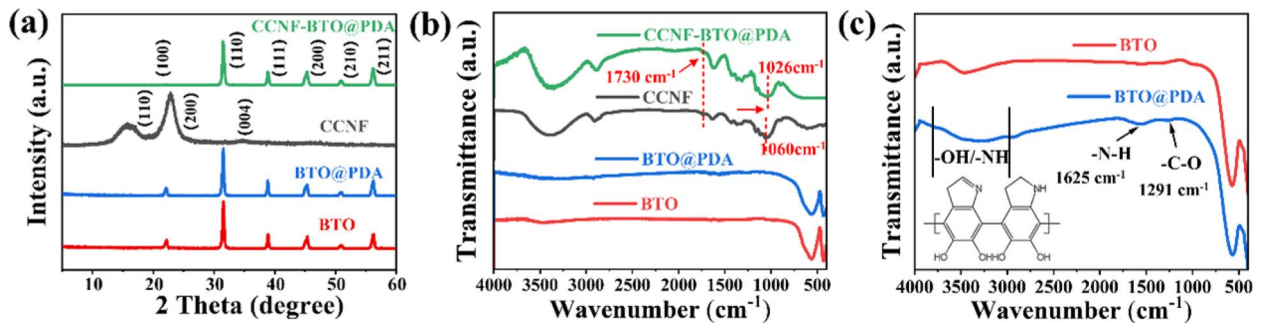


**Figure 4.** XRD and FTIR analysis of the nanoparticles. (a) XRD patterns of BTO, BTO@PDA, CCNF, and CCNF-BTO@PDA. (b,c) FTIR spectra of BTO, BTO@PDA, CCNF, and CCNF-BTO@PDA.

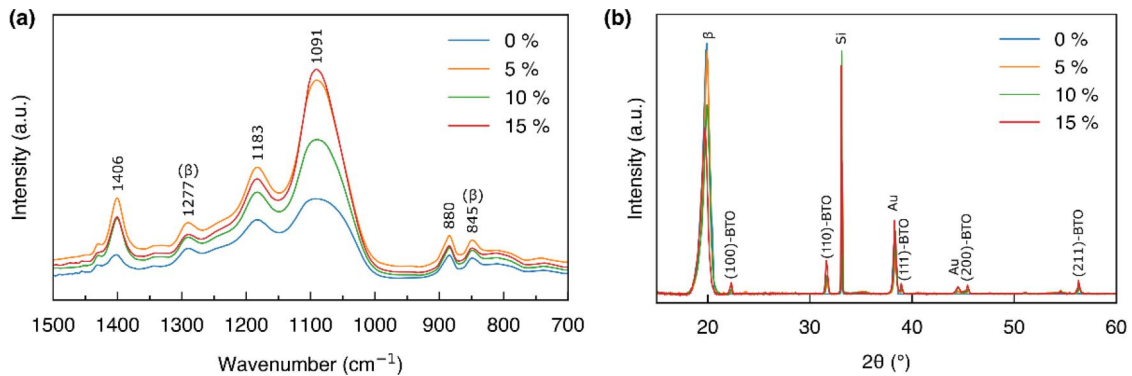


**Figure 5.** Chemical composition and crystalline phase of pure and nanocomposites P(VDF-TrFE) thin films. (a) FTIR spectrum (absorbance) and (b) XRD pattern with different nanofiller concentrations.

rocking modes of the *all-trans* conformation that is characteristic of the low-temperature phase of P(VDF-TrFE) (also called  $\beta$ -phase due to the similarity to the  $\beta$ -phase of pure PVDF). The typical  $\beta$ -phase peak at  $1073\text{ cm}^{-1}$  is likely masked by the high-intensity  $\text{SiO}_2$  peak at  $1091\text{ cm}^{-1}$ , determined by analyzing the pure silicon wafer. The absorption bands at  $880\text{ cm}^{-1}$ ,  $1183\text{ cm}^{-1}$ , and  $1406\text{ cm}^{-1}$  are instead barely sensitive to chain conformation, and both  $\alpha$ - and  $\beta$ -phase show the same total intensity [63]. Furthermore, contributions to these three bands from the IR absorption of the amorphous

phase cannot be excluded. Peaks related to the  $\alpha$ -phase, such as at  $763\text{ cm}^{-1}$ , have not been detected, probably due to the presence of the  $\text{SiO}_2$  layer, which exhibits another peak at  $795\text{ cm}^{-1}$  [64]. The overlap of the two peaks leads to an indistinct region, rendering the already low-intensity  $\alpha$ -peak unidentifiable [65]. Figure 5b shows the XRD patterns of both the pure P(VDF-TrFE) as well as the nanocomposite thin films, which were also subjected to FTIR analysis. At a  $2\theta$  value of  $19.7^\circ$ , we observe a diffraction peak corresponding to the (110) and (200) orientation plane of the pseudohexagonal

crystallographic microstructure of the low-temperature ferroelectric phase, commonly known as the  $\beta$ -phase [65]. However, there is a noticeable decrease in intensity as the weight percentage of CCNF-BTO@PDA nanofillers increases. This decrease in intensity suggests a reduced presence of the  $\beta$ -phase, indicating that the introduction of the nanoparticles is responsible for this crystallographic modification. While previous research demonstrated an increase in the  $\beta$ -phase content with the introduction of BTO@PDA in PVDF and P(VDF-TrFE) thin films [49,56], no reports have addressed the impact of introducing CCNF in P(VDF-TrFE). Although some studies on homopolymer PVDF suggest that introducing CCNF leads to the presence of the electroactive  $\gamma$ -phase, our observations primarily reveal a potential reduction in the ferroelectric  $\beta$ -phase for its copolymer P(VDF-TrFE) due to the presence of CCNF. Therefore, we propose that the introduction of CCNF influences the occurrence of the  $\beta$ -phase. Concerning the other diffraction peaks, a detailed comparison of Figure 5b with Figure 4a allows us to identify all peaks associated with the presence of BTO. Additionally, we detected also peaks at  $2\theta$  values of  $33^\circ$ ,  $38.2^\circ$ , and  $44.6^\circ$ , attributed to silicon and gold, representing the wafer substrate and the electrode material within the micromachined capacitors.

### Dielectric and energy storage performance of nanocomposite thin films

The dielectric constant of the nanocomposite thin films was measured as a function of the nanoparticle concentration using micromachined capacitors. As presented in Figure 6a, the permittivity at a measurement frequency of 100 Hz gradually increases almost linearly with the nanoparticle weight fraction, providing a significant advantage for energy storage applications [66] and demonstrating consistency with previous findings in similar

nanocomposite thin films [13]. Starting with a baseline permittivity of about 11 for pure P(VDF-TrFE), the introduction of BTO@PDA mixed with CCNF results in an increased dielectric constant, reaching a maximum value of 19 at 15% weight fraction. In Figure 6b, both the dielectric constant and the dielectric loss of the nanocomposite thin films at varying CCNF-BTO@PDA loadings are presented as a function of the measurement frequency. The decrease in dielectric permittivity is attributed to the dielectric relaxation of the P(VDF-TrFE) matrix. The dielectric loss, important when characterizing energy dissipation under an external field applied, shows minimal difference between the nanocomposite and the pure polymer thin films. With an increase in frequency, the dielectric loss increases due to the higher energy dissipation from polymer dielectric relaxation at higher frequencies [21]. The reported dielectric loss findings in this study align closely with previous research on P(VDF-TrFE) based and BTO@PDA nanofillers [67]. Using the same micromachined capacitors, the hysteretic response of the electric displacement  $D$  as a function of electric field  $E$  has been measured. In Figure 7,  $D$ - $E$  loops of the nanocomposite thin films, each with varying CCNF-BTO@PDA loadings, are presented and fitted with an empirical model developed by Miller et al. [68] (see Supplementary Figure 2). This fitting allowed us to extract parameters such as  $E_c$  and  $P_r$ . The resulting values are reported in Table 1 and further illustrated in Figure 8a. Notably, an increase in nanoparticle content results in a simultaneous decrease in both remnant polarization and coercivity, with the former decreasing more significantly than the latter. This observation is aligned with what we observed in the XRD patterns, indicating a decrease in the  $\beta$ -phase content with increasing nanofiller loadings, resulting in a reduction of the nanocomposite thin film electroactivity.  $E_c$  values remained relatively constant up to a weight fraction of 10%, consistent with typical values found in

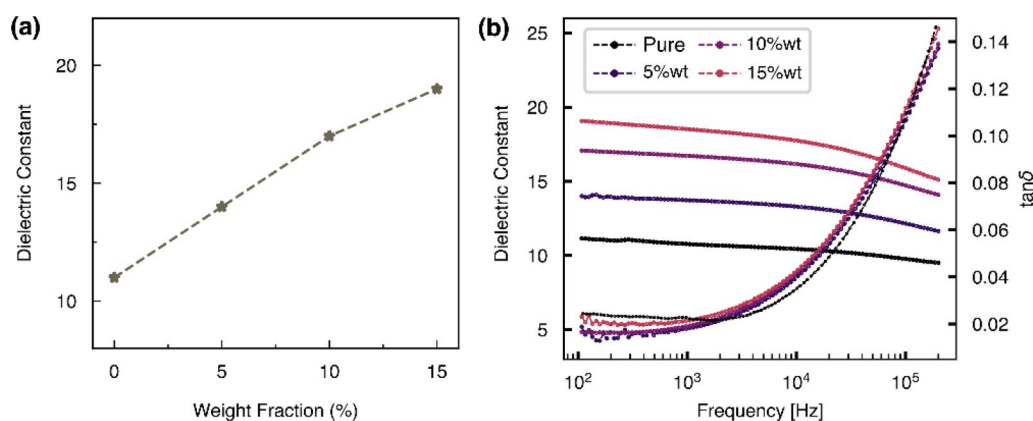


**Figure 6.** Dielectric characteristics of nanocomposite thin films. (a) Variation of dielectric constant with filler loading at 1 kHz. (b) The dielectric constant and dielectric loss of CCNF-BTO@PDA nanocomposites as a function of frequency at room temperature. The inserted straight lines serve as a guide to the eyes.

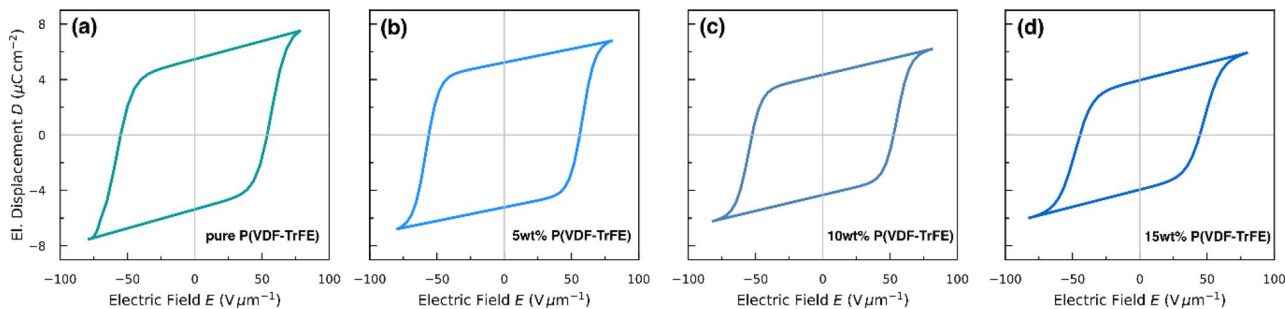


**Figure 7.** Ferroelectric characteristics of nanocomposite thin films. Electric displacement as a function of the electric field ( $D$ - $E$  hysteresis) of pure P(VDF-TrFE) (a) and nanocomposite thin films at various CCNF-BTO@PDA loadings (b–d).

**Table 1.** Coercivity and remnant polarization of the pure and the nanocomposite P(VDF-TrFE) thin films as a function of the nanofiller weight fraction.

| % weight fraction        | 0%  | 5%  | 10% | 15% |
|--------------------------|-----|-----|-----|-----|
| $E_c$ ( $V\mu m^{-1}$ )  | 57  | 56  | 55  | 48  |
| $P_r$ ( $\mu Ccm^{-2}$ ) | 5.6 | 5.1 | 4.4 | 4   |

the literature for pure P(VDF-TrFE) thin films [54,65,69]. However, a noticeable drop to  $48 V\mu m^{-1}$  was observed at 15%. As mentioned earlier, a more significant decrease has been found in the  $P_r$ , where the value dropped from  $5.6 \mu Ccm^{-2}$  for pure P(VDF-TrFE), in good agreement with values from the literature [54,65,69], to  $4 \mu Ccm^{-2}$  at a 15% weight fraction (Table 1 and Figure 8a). The reduction in  $P_r$ , combined with an optimized dielectric constant, contributes to an improved energy density in the material [10], as presented in Figure 8a. However, as previously mentioned, the use of such thin films with a thickness of about  $1 \mu m$  results in an increased presence of defects, which may lead to localized electrical breakdown. As a result, due to the limitations to applying extremely high electric fields, the energy storage values observed in our study are lower than those reported in the literature for thicker P(VDF-TrFE)- and PVDF-based films loaded with BTO, which can reach up values of  $5 J\cdot cm^{-3}$  [24,43]. Nevertheless, our research aims to demonstrate that energy storage applications can be achieved also at lower voltage fields by reducing the thickness and such thin films can still yield substantial improvements in energy storage properties through the introduction of nanofillers. Figure 8b illustrates the energy density and energy efficiency of the nanocomposite thin films at different CCNF-BTO@PDA loadings. The energy density has been calculated by integrating the area between the discharge curve and the ordinate [35] (See Supplementary Section 2). The energy efficiency is instead represented by the ratio between discharged and charged energies. Figure 8b shows that starting from an initial value in the pure P(VDF-TrFE) of  $0.58 Jcm^{-3}$  energy density and 14% energy efficiency, these parameters improved to  $0.92 Jcm^{-3}$  and 28%, respectively. Remarkably, the

P(VDF-TrFE) based nanocomposite with a 15% weight fraction of CCNF-BTO@PDA demonstrated a twofold increase in energy efficiency and nearly a 60% improvement in energy density.

## Conclusion

The study presents the synthesis of a nanoparticle mixture comprising carboxyl cellulose nanofibers and BTO coated with polydopamine nanoparticles, introduced into a P(VDF-TrFE) ferroelectric polymer matrix. Fabricated through the spin-coating method, the resulting nanocomposite thin films result in a thickness of  $\sim 1 \mu m$ , considerably thinner than the standard for energy storage characteristics studies which are typically about  $10 \mu m$  or even above. Remarkably, we achieved a nanofiller loading up to 15% weight fraction and conducted a comprehensive analysis of ferroelectric and energy characteristics. Despite the challenges associated with thinner layers, such as potential surface and bulk defects that could have a significant impact on the device performance compared to thicker films, adopting this fabrication technique enabled us to operate at lower voltages ( $\sim 150 V_{pp}$ ) than usually suggested in the literature, while still providing valuable insights for energy storage applications. FTIR and XRD analysis revealed no change in the crystalline phase from the pure P(VDF-TrFE) thin film. The chain conformation remained the ferroelectric  $\beta$ -phase, characteristic of P(VDF-TrFE). However, a reduction in peak intensity was observed with increasing nanoparticle loadings. This phenomenon has been addressed by the presence of the nanocellulose fibers, which, in contrast to their effect on homopolymer PVDF presented in previous publications, reduced the electroactivity of the polymer matrix. In the dielectric characteristics, we observed an almost linear increase in the dielectric constant as a function of CCNF-BTO@PDA loadings. The combination of the two effects brought by the introduction of the nanofillers, i.e. the reduction of the remnant polarization and an optimization dielectric constant, resulted in an improvement in energy

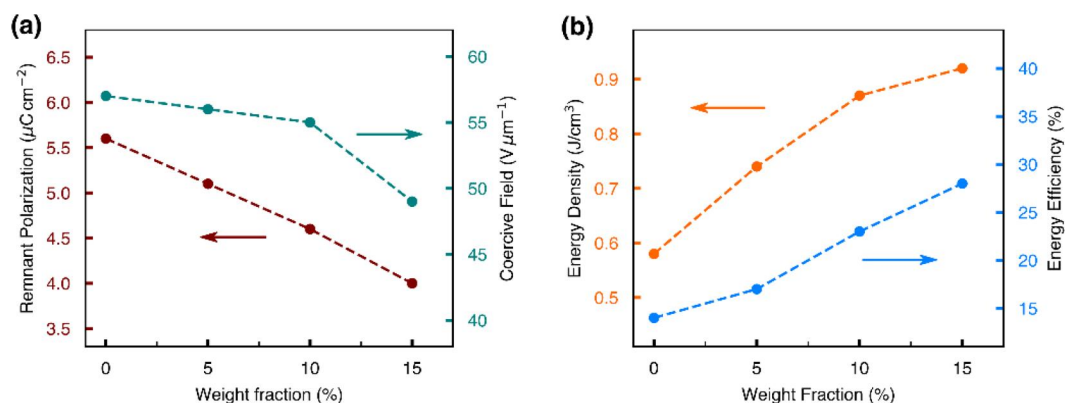


**Figure 8.** Ferroelectric and energy storage characteristics of the P(VDF-TrFE) thin films. (a) Variation of  $E_c$  and  $P_r$  (b) energy density and energy efficiency of P(VDF-TrFE) thin films at different CCNF-BTO@PDA loadings from 0% to 15% weight fraction. The inserted straight lines serve as a guide to the eyes.

storage characteristics. Compared to the pure P(VDF-TrFE), which exhibited an energy density of  $0.58 \text{ J cm}^{-3}$  and an energy efficiency of 14%, we enhanced these energy characteristics to  $0.92 \text{ J cm}^{-3}$  and 28%, respectively, with the 15% weight fraction CCNF-BTO@PDA nanocomposite thin film. Overall, we doubled the energy efficiency and improved the energy density by 60%. In conclusion, our study not only demonstrates the feasibility of achieving enhanced energy storage characteristics in thin films for lower voltage applications but also highlights the importance of nanofillers. This opens a new promising path for advancing the practical applications of P(VDF-TrFE) nanocomposite thin films at the micrometer range in energy storage devices.

## Acknowledgement

This project is funded by the Federal Ministry for Climate Action, Environment, Energy, Mobility, Innovation and Technology, BMK, and is carried out as part of the Production of the Future program. The authors acknowledge TU Wien Bibliothek for financial support through its Open Access Funding Program.

## Disclosure statement

No potential conflict of interest was reported by the author(s).

## Notes on contributors

**D. Disnan** studied Chemical and Materials Engineering at the University of Trieste, graduating in March 2019. In February 2020, he began his PhD at the Institute of Sensor and Actuator Systems at TU Wien, earning his degree in January 2025 with a thesis titled “Ferroelectric and energy storage characterization of electroactive polymer and nanocomposite thin films”. Since March 2025, he has been working as a postdoctoral researcher, focusing on NEMS and photothermal spectroscopy technology.

**M. Schneider** studied physics at the Karlsruhe Institute of Technology 2003–2009. He finished his studies in 2009 and started his PhD thesis on the optimization of ultra-thin aluminum nitride films for actuation and sensing applications in micro electromechanical systems at the Institute of Sensor and Actuator Systems (ISAS) at TU Wien. He received his PhD in 2014 and habilitated on the topic of piezoelectric silicon microsystems in 2021. Since 2022, he is head of the Christian Doppler Laboratory on Piezoelectric silicon MEMS with enhanced sensitivity and responsivity. Since 2023, he is Associate Professor at ISAS, where he focusses on material related aspects in piezoelectric materials and on advanced piezoelectric MEMS devices.

**Xinxin Zhang** graduated from College of Science, Shanghai University in June 2024 and is currently employed at Contemporary Amperex Technology Co., Limited (CATL) as a Cell Process Engineer, focusing on the improvement of cell manufacturing processes.

**Kunpeng Qian** graduated from School of Materials Science and Engineering, Shanghai University in June 2024 and is currently a lecturer of Packaging Engineering at the College of Food Science and Technology, Shanghai Ocean University, China. He specializes in intelligent packaging composite materials in the field of food preservation.

**F. Bacher** studied Electrical Engineering and Information Technology at TU Wien from 2020 to 2023. He completed his bachelor’s degree in 2023 with a thesis on “Energy storage and ferroelectric characterization of nanocomposite P(VDF-TrFE) thin films” at the Institute of Sensor and Actuator Systems (ISAS). Since 2023, he has been pursuing a master’s degree in Embedded Systems at TU Wien. His master’s thesis focuses on resonant MEMS sensors for detecting picogram latex-beads in liquids.

**Yin Zhao** is an Associate Professor at the College of Science, Shanghai University, China. Her research focuses on the design, controllable synthesis, and application of functional nanomaterials in various fields such as electronic functional ceramics, electrochemical energy storage, photoelectric conversion and catalysis.

**Xin Feng** is an Associate Professor at the College of Science, Shanghai University, China. He specializes in developing sustainable, biodegradable nanofibers, with a

focus on their synthesis, nanocomposite assembly, and physicochemical properties for lightweight, high-performance polymer composites.

*U. Schmid* started studies in physics at the University of Kassel in 1992. He performed his diploma work at the research laboratories of Daimler-Benz AG (now: Mercedes-Benz Group) on the electrical characterization of silicon carbide microelectronic devices. In 1999, he joined the research laboratories of EADS GmbH (now: Airbus Group) in Ottobrunn/Munich, Germany. From 2003 to 2008, he was Post-doc at the Chair of Micromechanics, Microfluidics/Microactuators at Saarland University. Since October 2008, he is full professor for Microsystems Technology at TU Wien heading since 2012 the Institute of Sensor and Actuator Systems. U. Schmid has authored or co-authored more than 450 peer-reviewed publications in journals and international conferences and holds more than 55 different granted patent families.

## References

1. Ahmad N, Ahmad SI, Ahmedi S, et al. Structural, optical and antifungal properties of the PMMA-ZnO nanocomposites: potential applications in odontology. *Mater Chem Phys.* 2023;309:128382. doi: [10.1016/j.matchemphys.2023.128382](https://doi.org/10.1016/j.matchemphys.2023.128382).
2. Pawar D, Kanawade R, Kumar A, et al. High-performance dual cavity-interferometric volatile gas sensor utilizing graphene/PMMA nanocomposite. *Sensors Actuators B Chem.* 2020;312:127921. doi: [10.1016/j.snb.2020.127921](https://doi.org/10.1016/j.snb.2020.127921).
3. Rafiefard N, Fardindoost S, Karimi Kisomi M, et al. High-performance flexible and stretchable self-powered surface engineered PDMS-TiO<sub>2</sub> nanocomposite based humidity sensors driven by triboelectric nanogenerator with full sensing range. *Sensors Actuators B Chem.* 2023;378:133105. doi: [10.1016/j.snb.2022.133105](https://doi.org/10.1016/j.snb.2022.133105).
4. Bodian S, Colchester RJ, Macdonald TJ, et al. CuInS<sub>2</sub> quantum dot and polydimethylsiloxane nanocomposites for all-optical ultrasound and photoacoustic imaging. *Adv Mater Interfaces.* 2021;8(20):2100518. doi: [10.1002/admi.202100518](https://doi.org/10.1002/admi.202100518).
5. Bai W, Lu Y, Hu Z, et al. Photoluminescence, thermal and surface properties of triarylimidazole-containing polyimide nanocomposite films. *RSC Adv.* 2021; 11(57):36066–36077. doi: [10.1039/d1ra07147e](https://doi.org/10.1039/d1ra07147e).
6. Kumar M, Kumari P. Design and fabrication of self-powered flexible P(VDF-TrFE)/ZnO/TiO<sub>2</sub> fiber mats as nanogenerator for wearable applications. *Mater Sci Semicond Process.* 2023;160:107429. doi: [10.1016/j.mssp.2023.107429](https://doi.org/10.1016/j.mssp.2023.107429).
7. Kumar M, Kumari P, Sahatiya P. P(VDF-TrFE)/ZnO nanofiber composite based piezoelectric nanogenerator as self-powered sensor: fabrication and characterization. *J Polym Res.* 2022;29:44. doi: [10.1007/s10965-022-02890-1](https://doi.org/10.1007/s10965-022-02890-1).
8. Kumar M, Kulkarni ND, Saha A, et al. Using multi-criteria decision-making approach for material alternatives in TiO<sub>2</sub>/P(VDF-TrFE)/PDMS based hybrid nanogenerator as a wearable device. *Sensors Actuators A Phys.* 2024;372:115331. doi: [10.1016/j.sna.2024.115331](https://doi.org/10.1016/j.sna.2024.115331).
9. Wang Y, Yao M, Ma R, et al. Design strategy of barium titanate/polyvinylidene fluoride-based nanocomposite films for high energy storage. *J Mater Chem A.* 2020;8(3):884–917. doi: [10.1039/C9TA11527G](https://doi.org/10.1039/C9TA11527G).
10. Thakur VK, Gupta RK. Recent progress on ferroelectric polymer-based nanocomposites for high energy density capacitors: synthesis, dielectric properties, and future aspects. *Chem Rev.* 2016;116(7):4260–4317. doi: [10.1021/acs.chemrev.5b00495](https://doi.org/10.1021/acs.chemrev.5b00495).
11. Bi M, Hao Y, Zhang J, et al. Particle size effect of BaTiO<sub>3</sub> nanofillers on the energy storage performance of polymer nanocomposites. *Nanoscale.* 2017;9(42): 16386–16395. doi: [10.1039/c7nr05212j](https://doi.org/10.1039/c7nr05212j).
12. Hou Y, Deng Y, Wang Y, et al. Uniform distribution of low content BaTiO<sub>3</sub> nanoparticles in poly(vinylidene fluoride) nanocomposite: toward high dielectric breakdown strength and energy storage density. *RSC Adv.* 2015;5(88):72090–72098. doi: [10.1039/C5RA10438F](https://doi.org/10.1039/C5RA10438F).
13. Hafner J, Schrattenholzer J, Teuschel M, et al. Modelling the distribution of BaTiO<sub>3</sub> nanoparticles in a P(VDF70-TrFE30) polymer matrix for permittivity calculation. *Polymer.* 2019;180:121682. doi: [10.1016/j.polymer.2019.121682](https://doi.org/10.1016/j.polymer.2019.121682).
14. Arshad AH, Dani S, Khanam BR, et al. Preparation, characterization, and electrical properties of PVDF-ZnO nanocomposite thin films. *J Mater Sci Mater Electron.* 2024;35(13):1–12. doi: [10.1007/s10854-024-12659-5](https://doi.org/10.1007/s10854-024-12659-5).
15. Behera R, Elanseralathan K. A review on polyvinylidene fluoride polymer based nanocomposites for energy storage applications. *J. Energy Storage.* 2022; 48:103788. doi: [10.1016/j.est.2021.103788](https://doi.org/10.1016/j.est.2021.103788).
16. Nelson JK, Fothergill JC. Internal charge behaviour of nanocomposites. *Nanotechnology.* 2004;15(5):586–595. doi: [10.1088/0957-4484/15/5/032](https://doi.org/10.1088/0957-4484/15/5/032).
17. Tamura R, Lim E, Manaka T, et al. Analysis of pentacene field effect transistor as a Maxwell-Wagner effect element. *J Appl Phys.* 2006;100:114515. doi: [10.1063/1.2372433](https://doi.org/10.1063/1.2372433).
18. Arshad AH, Dani S, Khanam BR, et al. Complex impedance and electric modulus of flexible ferroelectric polymer PVDF-ZnO hybrid nanocomposite thin films. *Polym Bull.* 2024;81(14):12755–12775. doi: [10.1007/s00289-024-05312-y](https://doi.org/10.1007/s00289-024-05312-y).
19. Feng M, Zhang C, Zhou G, et al. Enhanced energy storage characteristics in PVDF-based nanodielectrics with core-shell structured and optimized shape fillers. *IEEE Access.* 2020;8:81542–81550. doi: [10.1109/ACCESS.2020.2991058](https://doi.org/10.1109/ACCESS.2020.2991058).
20. Zhou T, Zha JW, Cui RY, et al. Improving dielectric properties of BaTiO<sub>3</sub>/ferroelectric polymer composites by employing surface hydroxylated BaTiO<sub>3</sub> nanoparticles. *ACS Appl Mater Interfaces.* 2011;3(7):2184–2188. doi: [10.1021/am200492q](https://doi.org/10.1021/am200492q).
21. Zhang X, Wang Y, Sheng Y, et al. Enhanced energy density in hydroxyl-modified barium titanate/poly(vinylidene-co-trifluoroethylene) nanocomposites with improved interfacial polarization. *Chem Phys Lett.* 2019;723:89–95. doi: [10.1016/j.cplett.2019.03.027](https://doi.org/10.1016/j.cplett.2019.03.027).
22. Chang SJ, Liao WS, Ciou CJ, et al. An efficient approach to derive hydroxyl groups on the surface of barium titanate nanoparticles to improve its chemical modification ability. *J Colloid Interface Sci.* 2009; 329(2):300–305. doi: [10.1016/j.jcis.2008.10.011](https://doi.org/10.1016/j.jcis.2008.10.011).
23. Ye HJ, Shao WZ, Zhen L. Tetradecylphosphonic acid modified BaTiO<sub>3</sub> nanoparticles and its nanocomposite. *Colloids Surfaces A Physicochem Eng Asp.* 2013; 427:19–25. doi: [10.1016/j.colsurfa.2013.02.068](https://doi.org/10.1016/j.colsurfa.2013.02.068).

24. Hu P, Gao S, Zhang Y, et al. Surface modified BaTiO<sub>3</sub> nanoparticles by titanate coupling agent induce significantly enhanced breakdown strength and larger energy density in PVDF nanocomposite. *Compos Sci Technol*. 2018;156:109–116. doi: [10.1016/j.compscitech.2017.12.025](https://doi.org/10.1016/j.compscitech.2017.12.025).
25. Yang D, Kong X, Ni Y, et al. Enhancement of dielectric performance of polymer composites via constructing BaTiO<sub>3</sub>-Poly(Dopamine)-Ag nanoparticles through mussel-inspired surface functionalization. *ACS Omega*. 2018;3(10):14087–14096. doi: [10.1021/acsomega.8b02367](https://doi.org/10.1021/acsomega.8b02367).
26. Liu Y, Ai K, Lu L. Polydopamine and its derivative materials: synthonal and promising applications in energy, environmental, and biomedical fields. *Chem Rev*. 2014;114(9):5057–5115. doi: [10.1021/cr400407a](https://doi.org/10.1021/cr400407a).
27. Lou Z, Tu Y, Yang Y, et al. An environmentally friendly and superhydrophobic melamine sponge self-roughened by in-situ controllably grown polydopamine nanoparticle for efficient oil-water separation. *Colloids Surfaces A Physicochem Eng Asp*. 2025;705(P1):135567. doi: [10.1016/j.colsurfa.2024.135567](https://doi.org/10.1016/j.colsurfa.2024.135567).
28. Li H, Yin D, Li W, et al. Polydopamine-based nanomaterials and their potentials in advanced drug delivery and therapy. *Colloids Surf B Biointerfaces*. 2021;199:111502. doi: [10.1016/j.colsurfb.2020.111502](https://doi.org/10.1016/j.colsurfb.2020.111502).
29. Lee H, Dellatore SM, Miller WM, et al. Mussel-inspired surface chemistry for multifunctional coatings. *Science*. 2007;318(5849):426–430. doi: [10.1126/science.1147241](https://doi.org/10.1126/science.1147241).
30. Park J, Brust TF, Lee HJ, et al. Polydopamine-based simple and versatile surface modification of polymeric nano drug carriers. *ACS Nano*. 2014;8(4):3347–3356. doi: [10.1021/nn405809c](https://doi.org/10.1021/nn405809c).
31. Zeng Y, Liu W, Wang Z, et al. Multifunctional surface modification of nanodiamonds based on dopamine polymerization. *Langmuir*. 2018;34(13):4036–4042. doi: [10.1021/acs.langmuir.8b00509](https://doi.org/10.1021/acs.langmuir.8b00509).
32. Wang Z, Wang T, Wang C, et al. Poly(vinylidene fluoride) flexible nanocomposite films with dopamine-coated giant dielectric ceramic nanopowders, Ba(Fe<sub>0.5</sub>Ta<sub>0.5</sub>)O<sub>3</sub>, for high energy-storage density at low electric field. *ACS Appl Mater Interfaces*. 2017;9(34):29130–29139. doi: [10.1021/acsami.7b08664](https://doi.org/10.1021/acsami.7b08664).
33. Cai W, Wang J, Pan Y, et al. Mussel-inspired functionalization of electrochemically exfoliated graphene: based on self-polymerization of dopamine and its suppression effect on the fire hazards and smoke toxicity of thermoplastic polyurethane. *J Hazard Mater*. 2018;352:57–69. doi: [10.1016/j.jhazmat.2018.03.021](https://doi.org/10.1016/j.jhazmat.2018.03.021).
34. Wang Y, Li J, Deng Y. Enhanced ferroelectricity and energy storage in poly(vinylidene fluoride)-clay nanocomposite films via nanofiller surface charge modulation. *RSC Adv*. 2015;5(104):85884–85888. doi: [10.1039/C5RA13456K](https://doi.org/10.1039/C5RA13456K).
35. Ghosh SK, Rahman W, Midya TR, et al. Improved breakdown strength and electrical energy storage performance of  $\gamma$ -poly(vinylidene fluoride)/unmodified montmorillonite clay nano-dielectrics. *Nanotechnology*. 2016;27(21):215401. doi: [10.1088/0957-4484/27/21/215401](https://doi.org/10.1088/0957-4484/27/21/215401).
36. Kausar A. Sustainable Nanocellulose and Nanohydrogels from Natural Sources, Chapter 17 - Nanocellulose in polymer nanocomposite. - *Micro and Nano Technologies*; 2020:357–366. doi: [10.1016/B978-0-12-816789-2.00017-1](https://doi.org/10.1016/B978-0-12-816789-2.00017-1).
37. Zheng W, Lv R, Na B, et al. Nanocellulose-mediated hybrid polyaniline electrodes for high performance flexible supercapacitors. *J Mater Chem A*. 2017;5(25):12969–12976. doi: [10.1039/C7TA01990D](https://doi.org/10.1039/C7TA01990D).
38. Fu R, Chen S, Lin Y, et al. Improved piezoelectric properties of electrospun poly(vinylidene fluoride) fibers blended with cellulose nanocrystals. *Mater Lett*. 2017;187:86–88. doi: [10.1016/j.matlet.2016.10.068](https://doi.org/10.1016/j.matlet.2016.10.068).
39. Lasrado D, Ahankari S, Kar K. Nanocellulose-based polymer composites for energy applications—a review. *J Appl Polymer Sci*. 2020;137(27):1–14. doi: [10.1002/app.48959](https://doi.org/10.1002/app.48959).
40. Rincón-Iglesias M, Lizundia E, Correia DM, et al. The role of CNC surface modification on the structural, thermal and electrical properties of poly(vinylidene fluoride) nanocomposites. *Cellulose*. 2020;27(7):3821–3834. doi: [10.1007/s10570-020-03067-z](https://doi.org/10.1007/s10570-020-03067-z).
41. Ruan M, Yang D, Guo W, et al. Improved dielectric properties, mechanical properties, and thermal conductivity properties of polymer composites via controlling interfacial compatibility with bio-inspired method. *Appl Surf Sci*. 2018;439:186–195. doi: [10.1016/j.apsusc.2017.12.250](https://doi.org/10.1016/j.apsusc.2017.12.250).
42. Xie Y, Yu Y, Feng Y, et al. Fabrication of stretchable nanocomposites with high energy density and low loss from cross-linked PVDF filled with poly(dopamine) encapsulated BaTiO<sub>3</sub>. *ACS Appl Mater Interfaces*. 2017;9(3):2995–3005. doi: [10.1021/acsami.6b14166](https://doi.org/10.1021/acsami.6b14166).
43. Zhang L, Wang Y, Xu M, et al. Multiple interfacial modifications in Poly(Vinylidene Fluoride)/Barium titanate nanocomposites via double-shell architecture for significantly enhanced energy storage density. *ACS Appl Energy Mater*. 2019;2(8):5945–5953. doi: [10.1021/acsaem.9b01052](https://doi.org/10.1021/acsaem.9b01052).
44. Sahu PK, Pandey RK, Dwivedi R, et al. Polymer/graphene oxide nanocomposite thin film for NO<sub>2</sub> sensor: an in situ investigation of electronic, morphological, structural, and spectroscopic properties. *Sci Rep*. 2020;10(1):2981. doi: [10.1038/s41598-020-59726-5](https://doi.org/10.1038/s41598-020-59726-5).
45. Lai S, Sublemontier O, Aubry E, et al. Aerosol-based functional nanocomposite coating process for large surface areas. *Sci Rep*. 2023;13(1):4709. doi: [10.1038/s41598-023-31933-w](https://doi.org/10.1038/s41598-023-31933-w).
46. Khorshidi B, Biswas I, Ghosh T, et al. Robust fabrication of thin film polyamide-TiO<sub>2</sub> nanocomposite membranes with enhanced thermal stability and anti-biofouling propensity. *Sci Rep*. 2018;8(1):784. doi: [10.1038/s41598-017-18724-w](https://doi.org/10.1038/s41598-017-18724-w).
47. Chen G, Zhao J, Li S, et al. Origin of thickness dependent DC electrical breakdown in dielectrics. *Appl Phys Lett*. 2012;100:222904. doi: [10.1063/1.4721809](https://doi.org/10.1063/1.4721809).
48. Tan DQ. The search for enhanced dielectric strength of polymer-based dielectrics: a focused review on polymer nanocomposites. *J Appl Polymer Sci*. 2020;137(33):1–32. doi: [10.1002/app.49379](https://doi.org/10.1002/app.49379).
49. Men T, Liu X, Jiang B, et al. Ferroelectric  $\beta$ -crystalline phase formation and property enhancement in polydopamine modified BaTiO<sub>3</sub>/Poly(vinylidene fluoride-trifluoroethylene) nanocomposite films. *Thin Solid Films*. 2019;669:579–587. doi: [10.1016/j.tsf.2018.11.051](https://doi.org/10.1016/j.tsf.2018.11.051).
50. Jin F, Xue X, Zhao Y, et al. Enhanced rate capability and high-voltage cycling stability of single-crystal nickel-rich cathode by surface anchoring dielectric BaTiO<sub>3</sub>. *J Colloid Interface Sci*. 2022;619:65–74. doi: [10.1016/j.jcis.2022.03.064](https://doi.org/10.1016/j.jcis.2022.03.064).

51. Ye S, Yu HY, Wang D, et al. Green acid-free one-step hydrothermal ammonium persulfate oxidation of viscose fiber wastes to obtain carboxylated spherical cellulose nanocrystals for oil/water Pickering emulsion. *Cellulose*. 2018;25(9):5139–5155. doi: [10.1007/s10570-018-1917-x](https://doi.org/10.1007/s10570-018-1917-x).
52. Chen G, Zhang C, Wang X, et al. Fabrication of tailored carboxymethyl-functionalized cellulose nanofibers via chemo-mechanical process from waste cotton textile. *Cellulose*. 2021;28(12):7663–7673. doi: [10.1007/s10570-021-03969-6](https://doi.org/10.1007/s10570-021-03969-6).
53. Li M, Katsouras I, Piliago C, et al. Controlling the microstructure of poly(vinylidene-fluoride) (PVDF) thin films for microelectronics. *J Mater Chem C*. 2013;1(46):7695–7702. doi: [10.1039/c3tc31774a](https://doi.org/10.1039/c3tc31774a).
54. Hafner J, Benaglia S, Richheimer F, et al. Multi-scale characterisation of a ferroelectric polymer reveals the emergence of a morphological phase transition driven by temperature. *Nat Commun*. 2021;12(1):1–9. doi: [10.1038/s41467-020-20407-6](https://doi.org/10.1038/s41467-020-20407-6).
55. Si H, Lee D, Park D, et al. Size effects of polydopamine-coated BaTiO<sub>3</sub> nanoparticles on the piezoelectric performance of P(VDF-TrFE)/BaTiO<sub>3</sub> composite. *J Mater*. 2024;10(4):857–869. doi: [10.1016/j.jmat.2023.10.006](https://doi.org/10.1016/j.jmat.2023.10.006).
56. Kumar M, Kulkarni ND, Kumari P. Piezoelectric performance enhancement of electrospun functionally graded PVDF/BaTiO<sub>3</sub> based flexible nanogenerators. *Mater Res Bull*. 2024;174:112739. doi: [10.1016/j.materresbull.2024.112739](https://doi.org/10.1016/j.materresbull.2024.112739).
57. Su Y, Li W, Yuan L, et al. Piezoelectric fiber composites with polydopamine interfacial layer for self-powered wearable biomonitoring. *Nano Energy*. 2021; 89(PA):106321. doi: [10.1016/j.nanoen.2021.106321](https://doi.org/10.1016/j.nanoen.2021.106321).
58. Tao J, Cao SA, Feng R, et al. High dielectric thin films based on barium titanate and cellulose nanofibrils. *RSC Adv*. 2020;10(10):5758–5765. doi: [10.1039/c9ra10916a](https://doi.org/10.1039/c9ra10916a).
59. Zhang K, Sun P, Liu H, et al. Extraction and comparison of carboxylated cellulose nanocrystals from bleached sugarcane bagasse pulp using two different oxidation methods. *Carbohydr Polym*. 2016;138:237–243. doi: [10.1016/j.carbpol.2015.11.038](https://doi.org/10.1016/j.carbpol.2015.11.038).
60. Yang Y, Pan H, Xie G, et al. Flexible piezoelectric pressure sensor based on polydopamine-modified BaTiO<sub>3</sub>/PVDF composite film for human motion monitoring. *Sensors Actuators A Phys*. 2020;301: 111789. doi: [10.1016/j.sna.2019.111789](https://doi.org/10.1016/j.sna.2019.111789).
61. Sehaqui H, Kulasinski K, Pfenninger N, et al. Highly carboxylated cellulose nanofibers via succinic anhydride esterification of wheat fibers and facile mechanical disintegration. *Biomacromolecules*. 2017;18(1): 242–248. doi: [10.1021/acs.biomac.6b01548](https://doi.org/10.1021/acs.biomac.6b01548).
62. Zhang H, Shi L, Feng X. Use of chitosan to reinforce transparent conductive cellulose nanopaper. *J Mater Chem C*. 2018;6(2):242–248. doi: [10.1039/C7TC03980H](https://doi.org/10.1039/C7TC03980H).
63. Arrigoni A, Brambilla L, Bertarelli C, et al. P(VDF-TrFE) nanofibers: structure of the ferroelectric and paraelectric phases through IR and Raman Spectroscopies. *RSC Adv*. 2020;10(62):37779–37796. doi: [10.1039/d0ra05478j](https://doi.org/10.1039/d0ra05478j).
64. Roosz N, Euvard M, Lakard B, et al. Synthesis and characterization of polyaniline-silica composites: raspberry vs core-shell structures. Where do we stand? *J Colloid Interface Sci*. 2017;502:184–192. doi: [10.1016/j.jcis.2017.04.092](https://doi.org/10.1016/j.jcis.2017.04.092).
65. Disnan D, Hafner J, Schneider M, et al. Spherulite-like microstructure observed for spin-cast P(VDF-TrFE) thin films and their ferroelectric characteristics. *Polymer*. 2023;272:125840. doi: [10.1016/j.polymer.2023.125840](https://doi.org/10.1016/j.polymer.2023.125840).
66. Zhang R, Li L, Long S, et al. Enhanced energy storage performance of PVDF composite films with a small content of BaTiO<sub>3</sub>. *J Mater Sci Mater Electron*. 2021; 32(19):24248–24257. doi: [10.1007/s10854-021-06890-7](https://doi.org/10.1007/s10854-021-06890-7).
67. Song Y, Shen Y, Liu H, et al. Enhanced dielectric and ferroelectric properties induced by dopamine-modified BaTiO<sub>3</sub> nanofibers in flexible poly(vinylidene fluoride-trifluoroethylene) nanocomposites. *J Mater Chem*. 2012;22(16):8063–8068. doi: [10.1039/c2jm30297g](https://doi.org/10.1039/c2jm30297g).
68. Miller SL, Nasby RD, Schwank JR, et al. Device modeling of ferroelectric capacitors. *J Appl Phys*. 1990; 68(12):6463–6471. doi: [10.1063/1.346845](https://doi.org/10.1063/1.346845).
69. Katsouras I, Asadi K, Li M, et al. The negative piezoelectric effect of the ferroelectric polymer poly(vinylidene fluoride). *Nat Mater*. 2016;15(1):78–84. doi: [10.1038/nmat4423](https://doi.org/10.1038/nmat4423).